Radiative characteristics and heat transfer regime transitions in CO2-based thermal plasma jets

Applied Thermal Engineering 298 (2026) 130994

Contents lists available at ScienceDirect

Applied Thermal Engineering

journal homepage: www.elsevier.com/locate/apthermeng

Research Paper

Radiative characteristics and heat transfer regime transitions in CO_2-based thermal plasma jets

Ibrahim Qasim *, Saumitra Mishra, Adrian Gunnarsson, Fredrik Normann, Klas Andersson

Department of Space, Earth and Environment, Chalmers University of Technology, Sweden

ARTICLE INFO

Keywords:
CO_2 thermal plasma
IR
Radiative intensity
Heat transfer

ABSTRACT

This experimental study examines the radiative heat transfer of CO_2-operated thermal plasma plumes based on axial measurements of radiative intensity. Narrow-Angle Radiometry (NAR) and Infrared Thermography (IR) were employed to characterize radiative intensity and plume morphology from a 300 kW_{el} plasma generator (PG) under varying arc current and CO_2 flow conditions. Peak intensities at 5 mm from the nozzle exceeded 100 kW/m^2·sr. Increasing arc current displaces the localized near-nozzle high-intensity emission zone axially while the NAR probes remain at fixed positions, such that the recorded intensities decrease not due to reduced plume energy but due to the shift in peak emission location. IR imaging confirmed that despite this decrease in line-of-sight radiative intensity, the plume remained thermally energetic, with detector counts from a tungsten reference rod placed downstream within the plasma plume increasing systematically with specific gas enthalpy, establishing a clear transition from radiation-dominated near-field heating to convection-dominated downstream energy transport. IR imaging shows a radial constriction of the plume referred to as necking, with neck diameters decreasing from 19 mm at 150 A to 6 mm at 300 A. An idealized spectral radiative transfer analysis is additionally presented, demonstrating how the measured NAR intensities can be used to examine possible gas temperature fields and CO_2 dissociation states consistent with the experimental observations. The results provide a well-defined experimental benchmark for future modelling of CO_2 plasma heat transfer in high-temperature industrial processes such as rotary kilns.

1. Introduction

Carbon dioxide (CO_2) emissions from fossil fuel use are a major driver of climate change, prompting global efforts to reduce atmospheric CO_2 through capture, storage, and conversion technologies [1,2]. Among CO_2 conversion methods, few can meet the extreme temperature demands of industrial processes like cement production, which relies on rotary kilns operating above 1400 °C. Conventional electrification options often lack the required temperature range or integration capability. Among emerging approaches, plasma-based processes have gained interest for their potential to enable high-temperature CO_2 utilization in industrial applications [3]. Thermal plasma systems offer a high-temperature, combustion-free solution, and using CO_2 as the plasma gas aligns with kiln process gases and may enhance radiative heat transfer. This raises interest in their potential for decarbonizing high-temperature industries. Plasma, an ionized gas composed of charged and neutral particles, is classified as either thermal or non-thermal based on its thermodynamic state [4,5]. Thermal plasmas, operating at high temperatures and near atmospheric pressure, are well suited for industrial applications due to their high energy density [6,7]. Unlike non-thermal plasmas, they can reach temperatures beyond 20,000 K, enabling effective CO_2 dissociation into reactive species such as CO and O_2 [8]. Thermal plasma torches are generally classified as transferred or non-transferred arc systems. In non-transferred torches, both electrodes are contained within the device, enabling stable and controlled high-temperature operation suitable for industrial environments [9]. Common working gases include argon, nitrogen, air, and hydrogen, selected based on their thermal conductivity, ionization potential, and chemical reactivity. CO_2, while less commonly used, offers unique advantages due to its strong infrared radiative properties and compatibility with industrial processes such as cement production [10]. The performance of CO_2-based thermal plasmas depends on factors like gas composition, arc current, and flow rate, all of which influence plume dynamics and heat transfer efficiency [11]. In particular, understanding the radiative properties and temperature distribution of the plasma jet is critical for estimating heat transfer to materials, such as the cement bed in a rotary kiln.

* Corresponding author.
E-mail address: ibrahim.qasim@chalmers.se (I. Qasim).

https://doi.org/10.1016/j.applthermaleng.2026.130994
Received 7 January 2026; Received in revised form 21 March 2026; Accepted 10 April 2026
Available online 13 April 2026

Nomenclature

I_{arc}	Arc current
U_{arc}	Arc Voltage
P_{in}	Input electrical power
P_{eff}	Effective power
R	Universal gas constant
T	Bulk temperature
Mw	Molecular mass
Q_{loss}	Cooling water heat loss
M	Mach number
h_{fg}	Flue gas enthalpy

Greek symbols

η	Electro-thermal efficiency
ε	Emissivity
γ	Adiabatic index for CO_2

Acronyms

CFD	Computational fluid dynamics
DAQ	Data acquisition
HVHF	High-voltage high-frequency
IR	Infrared thermography
NAR	Narrow-angle radiometer
PG	Plasma generator

Several researchers have focused on estimating temperatures from thermal plasma torches for various applications. Wang et al. [12] investigated the characteristics of a DC plasma torch with multiple cathodes operating at atmospheric pressure using helium as the plasma gas for the application of zirconia spray coating. Plasma plume temperatures were measured using a water-cooled probe, which monitored cooling water temperature changes to calculate the specific enthalpy and core temperature of the plasma. With arc current and power held constant, they observed a decrease in core temperature from 19,330 K to 16,020 K as the gas flow rate increased from 15 standard liters per minute (slm) to 35 slm. Hrabovsky et al. [13] designed a water-stabilized DC arc plasma torch for the gasification of biomass and plastics using CO_2 as the plasma gas. The bulk plasma temperature (~15,500 K) was estimated using calorimetric measurements, while thermocouples were employed to monitor the reactor wall and syngas temperatures before quenching. Amarnath et al. [14] developed a DC non-transferred arc thermal plasma torch using a mixture of CO_2, Ar, and CH_4 for material processing under atmospheric pressure. Plasma temperatures were estimated using optical emission spectroscopy and ranged from 13,400 K to 17,800 K with varying discharge currents. Yang et al. [15] explored CO_2 pyrolysis in a double-anode thermal plasma reactor with a novel supersonic quenching system. The system achieved pyrolysis gas temperatures up to 3050 K and a rapid quenching rate of 10^7 K/s to prevent reverse reactions. Yugeswaran et al. [16] investigated the characteristics of a DC argon plasma plume generated using a non-transferred arc plasma spray torch. The plasma plume temperatures (6500–9200 K) were measured using the atomic Boltzmann plot method. Galaly et al. [17] conducted an experimental investigation into the operational characteristics of air plasma torches for plastic waste gasification, achieving plasma plume temperatures between 15,000 K and 19,000 K at flow rates of 10–30 g/s.

Numerous modelling studies have also been conducted to study the temperature fields and heat transfer conditions from thermal plasmas. Villarreal-Medina et al. [18] conducted numerical modelling to study heat transfer mechanisms in electric arcs of various gases, including CO_2, at atmospheric pressure. They identified the arc column, defined as the central, highly ionized region of the plasma discharge between the electrodes, as the primary zone for energy transfer, with radiation being the dominant heat transfer mechanism in CO_2 plasmas under these conditions. Zhou et al. [19] investigated thermal plasma gasification of solid waste using a DC non-transferred arc plasma torch. By analyzing the plasma system temperature distribution through numerical simulations using Fluent, core temperatures of up to 4300 K were estimated, enabling efficient gasification and heavy metal encapsulation in amorphous slag. Murphy et al. [20] modelled thermal plasma processes, highlighting two-way interactions between the plasma and the processed material. They demonstrated that the surface properties significantly influenced plasma heat transfer, emphasizing the need for accurate modelling of radiative and conductive heat transfer. Ko et al. [21] conducted a computational fluid dynamics (CFD) study, utilizing a DC non-transferred arc thermal plasma torch integrated into a cement kiln to improve sulphur hexafluoride pyrolysis efficiency. The plasma plume was shown to provide local high temperatures exceeding 5000 K at the torch exit, stabilizing the kiln's internal temperature and enhancing pyrolysis by promoting uniform heat distribution. Bonizzoni and Vassallo [22] explored the use of non-transferred thermal plasma at 6 MW for hazardous waste destruction, employing pyrolysis and vitrification that achieve temperatures of over 10,000 K. Zhang et al. [23] developed a numerical model to analyze heat transfer mechanisms in a composite arc plasma system combining cold metal transfer and pulse techniques. The study revealed a correlation between temperature distribution, current density, and electrode distance, showing local temperature peaks exceeding 8000 K near the anode. Gleizes et al. [24] conducted a comprehensive review of thermal plasma modelling, focusing on heat transfer, radiation, and chemical kinetics in DC arcs. Their findings highlighted the dominant role of radiation in energy loss and heat transfer in plasma arcs at temperatures exceeding 15,000 K, and roughly 90% of resonance-line photons emitted by the arc core are reabsorbed within the first millimeter of plasma radius; as the optical depth rises, the net emission coefficient therefore drops by about two orders of magnitude.

In high-temperature thermal processes such as rotary kilns for cement production and glass-melting furnaces, heat transfer to the processed material arises from a combination of radiative exchange and convective transport by hot gases [25]. The relative contribution of these mechanisms depends strongly on plume structure, spatial energy distribution, and the degree of enclosure. When electrically driven plasma heating is considered as an alternative to conventional combustion, the manner in which energy is released and transported along the plume may differ substantially; however, how radiative and convective heat-transfer regions develop along plasma jets under realistic operating conditions remains insufficiently characterized. In enclosed industrial systems, wall reflections, re-radiation, and view-factor effects further complicate the effective heat-transfer field. A detailed, spatially resolved understanding of plume-scale heat-transfer behavior is therefore required to assess how plasma torches can be integrated into industrial thermal processes and how burner placement, refractory design, and operating conditions should be selected. While previous studies have estimated plasma temperatures using different measurement techniques and modelling approaches, detailed experimental data on radiative heat transfer in CO_2 thermal plasma systems remain scarce. Specifically, there is a limited understanding of how operational parameters such as current and gas flow influence radiative intensity profiles and plume geometry, especially across different power scales. Existing literature tends to focus on plasma diagnostics without addressing how radiative energy is spatially distributed.

This paper experimentally studies CO_2-based thermal plasma plumes, using narrow-angle radiometry and infrared imaging to examine how the radiative intensity and thermal morphology change with electrical power and CO_2 flow rate. The findings contribute to the understanding of heat transfer mechanisms in high-temperature industrial applications. A “necking phenomenon” was observed during the experimental work, and possible causes and effects are discussed. In

addition, the data presented here offer a robust basis for developing or validating advanced numerical models of heat transfer and plasma behavior in high-power CO_2 jet plumes.

2. Experimental setup and measurement techniques

This section presents the experimental setup, measurement instruments, and test conditions used to investigate the radiative behavior of CO_2-based thermal plasma plumes. A thermal plasma torch of 300 kW_{el} was used to study plume geometry, axial radiative intensity, and infrared emission under varying arc currents and gas flow rates. The setup integrates narrow-angle radiometry (NAR) and infrared thermography (IR) to enable spatially resolved, non-intrusive characterization of the plume's radiative and morphological properties.

2.1. Experimental setup

A customized DC 300 kW_{el} non-transferred arc plasma torch operating was used to generate CO_2 plasma plumes in open air. The plasma torch used in this study is a DC hollow electrode plasma generator, consisting of a copper cathode and anode configuration separated by an insulating spacer. The electrodes are water-cooled to maintain thermal stability during operation, with cooling channels arranged to ensure effective heat dissipation across the system. A high-voltage, high-frequency (HVHF) igniter initiates the arc discharge by creating a pilot arc at a controlled CO_2 gas flow rate. The plasma arc is stabilized by the controlled feed of CO_2 as the working gas, using a gas flow controller. The anode diameter and nozzle outlet diameter for the 300 kW_{el} torch were 70 mm and 20 mm, respectively. A schematic view of the 300 kW_{el} plasma torch and experimental setup is shown in Fig. 1.

The operational parameters used for the 300 kW_{el} plasma torch are presented in Table 1. In the experiments, the arc current and CO_2 gas flow were set as control variables, while the arc voltage established itself dynamically during operation. The electrical input power is calculated as:

Table 1
Plasma torch operating parameters for the 300 kW_{el} (P1–P10) cases.

Case Id	Current (A)	Voltage (V)	Gas flow (Nm^3/h)	Efficiency η (%)	P_{in} (kW)
P1	100	1000	30	–	100
P2	150	930	30	89	140
P3	150	1020	40	89	153
P4	200	950	40	87	190
P5	250	920	40	86	230
P6	200	1030	50	87	206
P7	250	995	50	86	249
P8	300	975	50	85	293
P9	250	1038	55	86	260
P10	300	1000	55	85	300

$$P_{in} = U_{arc}.I_{arc} \tag{1}$$

The electro-thermal efficiency (η) of the torch is determined by measuring the heat losses through the cooling water and is expressed as:

$$\eta = \frac{P_{in} - Q_{loss}}{P_{in}} \times 100 \tag{2}$$

During the experiments, the plasma plume exited the PG outlet and propagated axially in open air. In the 300 kW_{el} system, four narrow-angle radiometers (NAR) were placed at axial positions of 5 mm, 50 mm, 105 mm, and 162 mm from the PG outlet to measure radiative intensity perpendicular to the plume. A tungsten rod was used as a reference target for temperature measurements, placed at the far end of the 300 kW_{el} plasma system (256 mm from the PG outlet) in a region where extreme heat would not cause material melting. This positioning provided a reliable point of comparison and ensured that temperature data could be captured near the arc's tail.

An infrared (IR) camera was used to capture the thermal profile of the plasma plumes. The camera was aligned with the axis of the second NAR probe from the PG outlet (50 mm). This strategic placement allowed simultaneous measurement of radiative intensity and visually

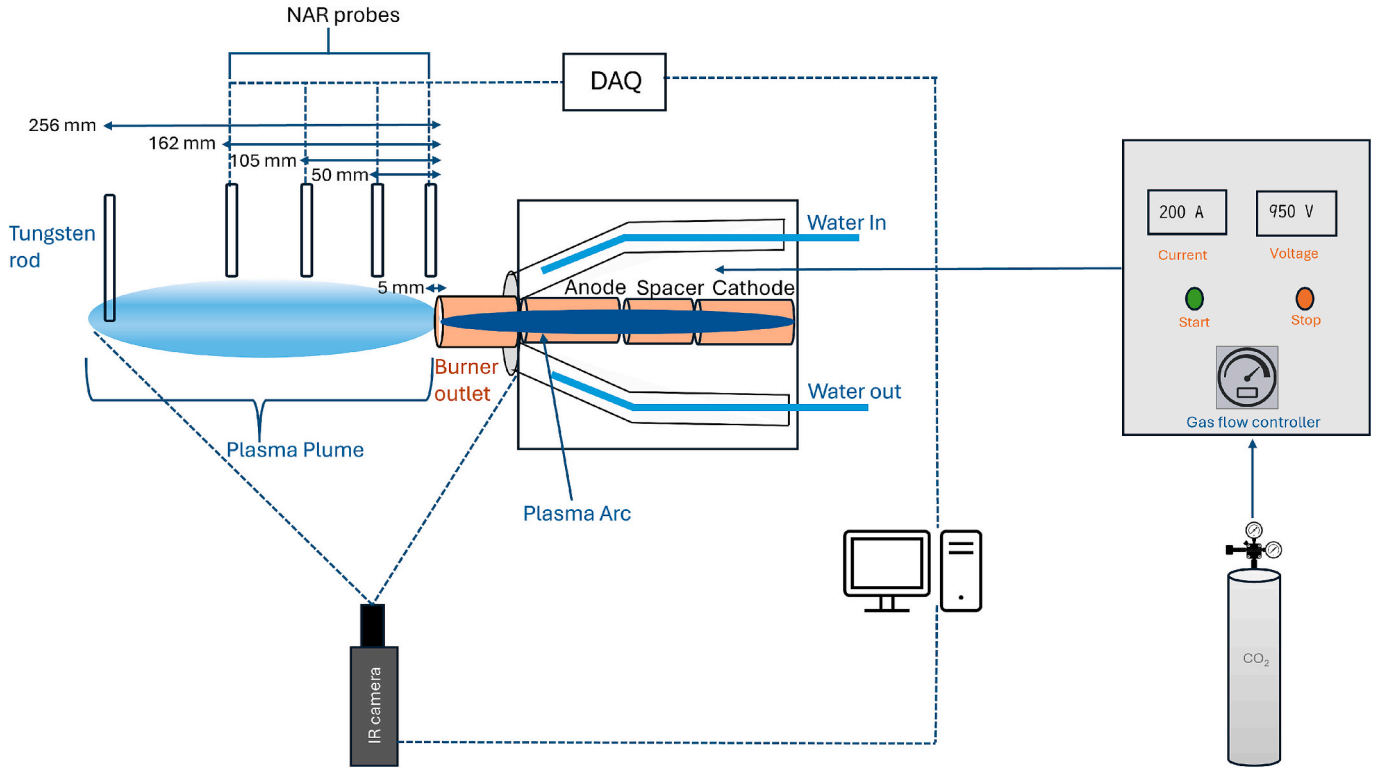

Fig. 1. Schematic of 300 kW_{el} thermal plasma torch and experimental setup. DAQ = Data AcQuisition, NAR = Narrow Angle Radiometer.

capturing the plasma plume, facilitating a comprehensive analysis of heat transfer characteristics.

2.2. Measurement techniques

NAR measured the radiative intensity of the plasma plume at multiple axial positions. They are designed to measure the radiative intensity in the probe's direct line of sight, with internal threading on the tube wall to eliminate stray reflections and ensure accurate intensity readings. For each probe, incident radiation is measured by a 2 M Thin Film Based Thermopile Detector, a broadband thermal detector that operates based on the Seebeck effect. This principle involves temperature differences across thermocouples generating a measurable voltage signal. The detector's fast response time, ranging from 0.01 to 0.1 s, ensures it can capture dynamic variations in radiative intensity, as encountered in plasma experiments. The detector's sensitivity is optimized for broadband detection, capturing a wide range of wavelengths typically encountered in high-temperature flames and gases. The thermopile detector has a high signal-to-noise ratio, with typical values around 19,500 $\sqrt{\text{Hz}}$, ensuring that even weak radiative intensities are measured accurately. It also features low thermal mass, contributing to its rapid response and high thermal sensitivity, with operational reliability across a wide temperature range. Assuming the detector as a disc with the same area as the actual detector: $R = 1{,}13$ mm, the instrument has a very narrow view angle corresponding to a solid angle of 9.45×10^{-5} sr. The narrow solid angle of the NAR probe restricts the measurement to a small line-of-sight volume, providing high spatial selectivity but making the measured intensity sensitive to plume geometry and alignment. As a result, the NAR data captures localized radiative emission rather than integrated plume radiation. The thermopile detector was calibrated before and after the experimental campaign using a Landcal R1500T precision blackbody furnace, with temperatures up to 1500 °C. Calibration ensured the voltage signal produced by the detector corresponded accurately to radiative intensity values. Radiative intensity signals from the NAR probes were sampled at 10 Hz and time-averaged over approximately 60 s of steady operation at each axial position. Mean values are reported in the main text, while minimum and maximum values corresponding to a 95% confidence interval are provided in the Supporting material (Table S1).

A FLIR A655SC thermal imaging camera, factory calibrated, was utilized to visually capture the plasma plume and temperature distribution. The camera provides a resolution of 640 × 480 pixels and operates at a sampling frequency of 50 Hz with a spectral sensitivity range of 7.5–14 μm, optimized for detecting infrared radiation emitted by high-temperature processes. However, it is not specifically designed for detecting gas radiation, as many gases have absorption/emission bands outside this spectral range or require higher spectral resolution for reliable identification. The FLIR A655SC series camera is capable of measuring temperatures up to 2000 °C, and a measurement accuracy of ±2 °C of the reading. The measurements were recorded at a fixed emissivity value setting of 0.2 in the camera software, chosen both to avoid saturation of the IR signal and because CO_2 gas is known to have a relatively low effective emissivity in the mid-IR spectral range. A high threshold preset with shorter integration and calibrated optical attenuation was used, yielding lower counts from cooler regions. Infrared measurements were recorded continuously for approximately 2 min at steady operating conditions. IR thermography provides spatially resolved qualitative information on plume geometry and downstream heating, while quantitative interpretation is limited by emissivity uncertainty and camera calibration limits.

A key geometric feature of the plasma plume, referred to as necking, was observed during high-current operation, characterized by a localized radial constriction in the plume profile. Necking geometry, further explained in the Results & Discussion section, was quantified using the captured IR thermograms during operation, where the thickness of the neck sections was estimated by extracting 500 individual frames per case. These frames were converted in a post-processing sequence into binary images in MATLAB, and the plasma plume diameter was evaluated across the entire axial length of the plume in each frame. The narrowest width, representing the minimum plume diameter, was recorded for each frame and averaged across all 500 frames to obtain a representative neck thickness. This method ensured statistical robustness and accounted for fluctuations in plasma plume geometry. Prior to plasma operation, spatial calibration was performed by capturing a reference thermograph of the burner and probe assembly without plasma, using the known physical distance between the burner and probes to convert pixel values to physical dimensions.

2.3. Measurement uncertainty and limitations

The uncertainties associated with the present measurements arise from a combination of instrumental, geometric, and physical factors. Instrumental uncertainty in the narrow-angle radiometry (NAR) measurements originates from detector calibration, electronic noise, and short-time signal fluctuations. To address this, radiative intensity signals were time-averaged under steady operating conditions, and statistical ranges based on 95% confidence intervals are reported. Average, minimum, and maximum values for all axial positions and operating cases are provided in the Supporting Information. Additional uncertainty arises from the highly localized nature of the NAR measurements. The probes collect radiation over a very narrow solid angle ($\sim 10^{-5}$ sr), making the measured intensity sensitive to plume geometry, alignment, and radial displacement of the most radiative regions. As a result, local changes in plume structure can lead to pronounced variations in the recorded signal even when the overall thermal state of the plasma remains high.

Infrared thermography provides complementary spatial information but is subject to uncertainty related to gas emissivity, detector sensitivity, and optical attenuation settings. For this reason, IR data are used primarily for qualitative interpretation of plume geometry and downstream heating behavior, while quantitative interpretation focuses on detector counts rather than absolute temperatures. Despite these uncertainties, the relative axial trends, the ordering of cases based on specific gas enthalpy, and the systematic evolution of plume constriction with arc current are robust and reproducible across the dataset. These trends form the basis for the physical interpretation presented in this work.

3. Results & discussion

3.1. Axial radiative intensity measurements

Radiative intensity measurements provide the most direct assessment of how thermal energy is distributed along the CO_2-based plasma plumes. The radiative intensity measured by the narrow-angle radiometers represents a line-of-sight quantity rather than the total radiative power emitted by the plasma plume. The recorded signal, therefore, depends not only on local temperature but also on the spatial extent of the emitting volume, plume geometry, and optical depth along the viewing path. In high-temperature CO_2 plasmas, radiation from the dense arc core is partly reabsorbed within the plasma itself, while the net emission detected externally reflects an effective radiative layer whose position and thickness may vary with operating conditions. Fig. 2(a) and (b) present axial intensity profiles of the 300 kW_{el} plasma cases (P1–P10), where the dataset is divided into two sub-figures for visual clarity and readability. The probe positions used for each dataset are indicated in the figure.

The 300 kW_{el} plasma cases displayed a markedly non-linear intensity profile (Fig. 2a and b). At 5 mm downstream of the nozzle, peak values exceeded 100 $kW/m^2 \cdot sr$, which likely reflects the proximity to the arc column and may indicate that the arc extends partially beyond the torch exit under certain operating conditions. However, at 50 mm, measured

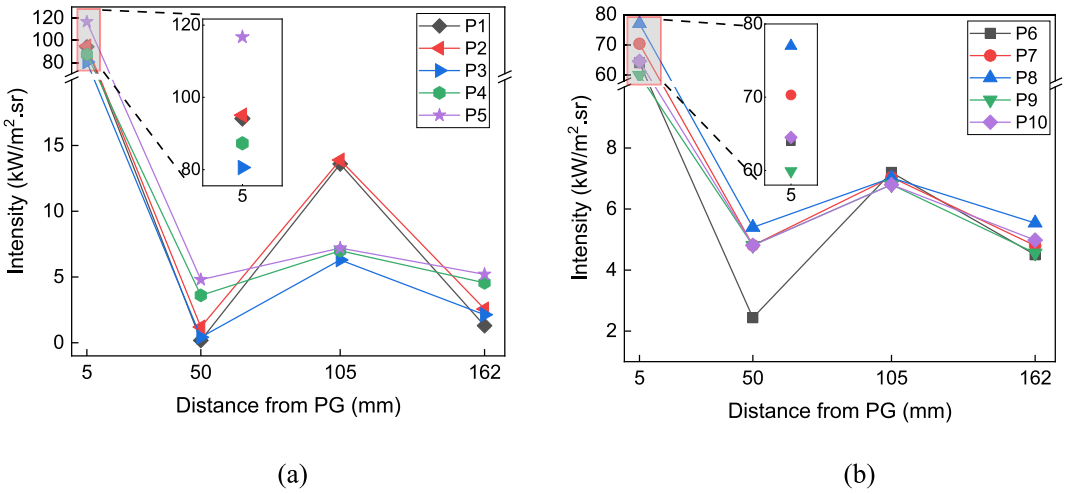

Fig. 2. Axial radiative intensity measurements. (a) Radiative intensity profiles for 300 kW_{el} plasma generator cases (P1–P5) (b) Radiative intensity profiles for 300 kW_{el} plasma generator cases (P6–P10).

intensities dropped sharply to 2–6 kW/m^2·sr, followed by a partial recovery to around 8–10 kW/m^2·sr further downstream at 105 and 162 mm. This sudden decrease near 50 mm cannot be explained solely by energy loss, as IR imaging confirms that the plasma plume remains luminous and the tungsten rod further downstream at 256 mm glows strongly. Instead, the drop is considered associated with an observed necking phenomenon described in the following section, where the plume contracts radially and reduces the overlap between the most radiative zone and the probe's narrow line of sight. The plasma continues to emit radiation as hot gases pass through this region; a larger fraction of the emission falls outside the probe's narrow solid angle, so the recorded value decreases even if the plume remains hot. The effective view angle of the probe is extremely narrow, corresponding to a solid angle on the order of 9.5×10^{-5} sr. Consequently, even small radial displacements of the hottest emission zone can appear as large drops in measured intensity. As the plume re-expands further downstream, the measured intensity stabilizes at modest but consistent levels. This behavior reflects how plume geometry affects the NAR line-of-sight measurements. Since the probe samples only a narrow viewing cone and cannot be repositioned during operation, shifts in the hottest emission zone may appear as reduced intensity, even though the plasma continues to emit strongly. The variation of peak radiative intensity with gas enthalpy (Fig. 3) further illustrates how the plasma heating zone can shift depending on operating conditions. The specific enthalpy of the plasma gas was calculated by dividing the effective power input to the gas by the volumetric flow rate of CO_2 at normal conditions.

$$h_{gas} = \frac{P_{eff}}{V_{CO_2}} \left(\frac{\text{MJ}}{\text{Nm}^3}\right) \tag{3}$$

$$P_{eff} = P_{in-} Q_{loss} \tag{4}$$

This yields the average energy delivered per unit volume of gas. Although higher input power should increase total energy, the maximum measured radiative intensity does not scale with enthalpy. Instead, the probe location relative to the brightest emission region becomes decisive. At some operating conditions, the probe positioned at 5 mm captures the hotspot directly; at others, the emission maximum is displaced axially or radially, reducing the measured value. These results highlight the need for high spatial resolution when characterizing heat transfer in plasma jets, as local geometry and flow strongly influence both radiation and convection.

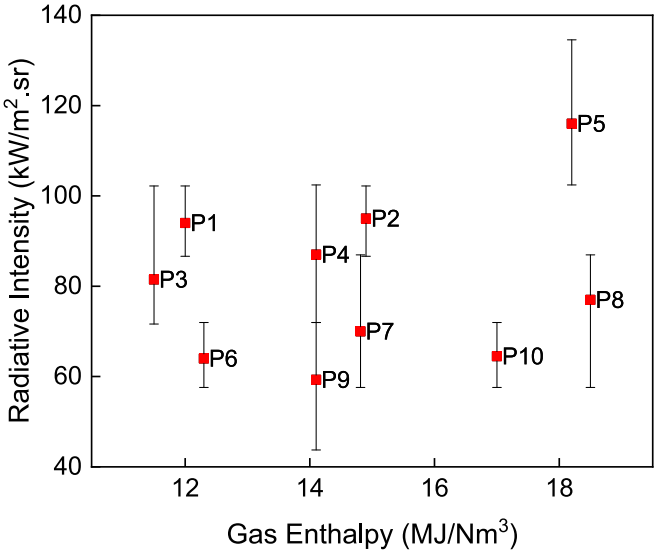

Fig. 3. Peak radiative intensity at 5 mm from the burner versus gas enthalpy (300 kW_{el} cases). Red squares mark the mean; error bars show the 95% confidence range (minimum–maximum) recorded for each case. (For interpretation of the references to colour in this figure legend, the reader is referred to the web version of this article.)

3.2. Infrared imaging

Infrared (IR) imaging served as the principal tool for visualizing the overall geometry and spatial evolution of the most radiative region of the CO_2-based plasma plume under different currents (100–300 A) and gas flow rates (30–55 Nm^3/h). For clarity, four representative operating cases (P1, P3, P5, and P8; see Table 1) are presented in Fig. 4 to illustrate the systematic morphological transition observed across the dataset. The plasma generator outlet is placed in line with the right end of each subfigure. The remaining cases are provided in the Supporting Information (Fig. S1). All images are shown at identical spatial and colour scales to enable direct comparison.

In each image, a glowing solid object is visible near the downstream end of the plume; this is the tungsten rod used as a reference target, which appears brighter than the surrounding plasma, indicating its high surface temperature. The NAR probes can also be seen in the images, along with faint purple rings surrounding the core of the plume.

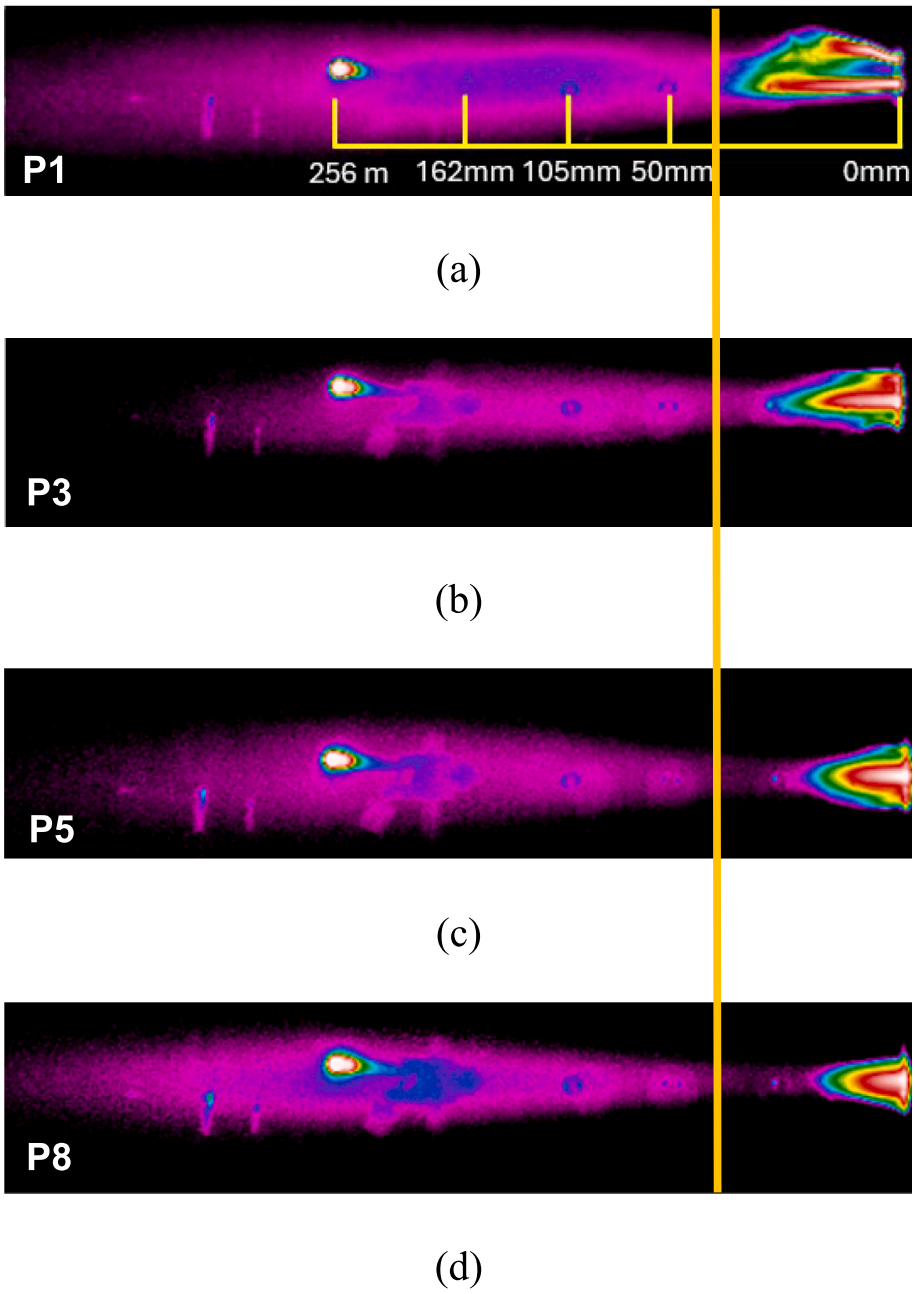

Fig. 4. Infrared thermograms of representative CO_2-based plasma plumes (300 kWel cases P1, P3, P5, and P8; see Table 1). All images are shown at identical spatial and colour scales. The plasma generator outlet is located at the right edge of each panel. The yellow contour delineates the boundary of the most intense radiative core, illustrating its axial displacement and radial confinement with increasing arc current. The tungsten reference rod and NAR probe positions are visible downstream. (For interpretation of the references to colour in this figure legend, the reader is referred to the web version of this article.)

At the lowest current (P1, 100 A, 30 Nm^3/h), the plume exhibits a relatively diffuse and irregular radiative region near the nozzle exit, with a broader luminous envelope. Increasing the current to 150 A (P3) results in a more defined and axially elongated hot region, indicating improved arc stability and increased energy concentration near the core. At 250 A and 40 Nm^3/h (P5), the near-nozzle radiative core becomes more intense and spatially confined, while the downstream plume remains thermally luminous, suggesting stronger convective transport of heated gas. At the highest current level of 300 A (P8, 50 Nm^3/h), the thermogram reveals a pronounced axial confinement of the hottest radiative zone immediately downstream of the nozzle, accompanied by a distinct radial constriction. The highlighted contour marking the most radiative region demonstrates that the effective emission core shifts closer to the nozzle and becomes more concentrated as the current increases.

Beyond the constricted near-field region, all high-current cases show an extended luminous plume persisting far downstream of the burner. Although the most intense radiative emission is concentrated close to the nozzle, the downstream thermograms confirm that substantial thermal energy remains within the jet and is transported axially by convection, as discussed in the next paragraph. This observation provides direct visual support for the axial radiative intensity measurements. While line-of-sight intensity decreases at intermediate probe positions due to geometric and optical effects, the plume remains thermally energetic, and heat continues to be delivered downstream. Taken together, the IR thermograms demonstrate that increasing arc current alters the spatial energy distribution within the plume, concentrating radiative emission in the near field while maintaining substantial convective transport

downstream.

To complement the qualitative thermograms, the digital counts recorded at the tungsten rod were extracted for all 300 kW_{el} cases (Table 2). Detector counts and apparent temperatures were obtained by time-averaging the recorded signal to ensure that the reported values represent statistically stable plume behavior rather than transient fluctuations. Because the tungsten rod is a solid body exposed to the plasma flow, its heating results from the combined effects of convective heat transfer from the hot gas and radiative re-emission from the heated surface. The counts represent the raw detector signal and remain invariant with respect to set material emissivity; they therefore provide the most robust, assumption-free indicator of the radiative flux emitted from the rod. When the cases are grouped by specific gas enthalpy, a clear pattern emerges. The lowest-enthalpy cases (P1, P3, P6) correspond to the lowest count levels, the intermediate-enthalpy cases (P2, P4, P7, P9) give intermediate counts, and the highest-enthalpy cases (P8 and P10) exhibit the largest counts. Case P5 gives a mid-range count level despite its comparatively strong near-field radiative intensity, consistent with a larger fraction of energy being emitted upstream close to the burner and less reaching the tungsten rod. These trends reflect how electrical loading shapes the enthalpy groups: at fixed gas flow, increasing the arc current increases the specific gas enthalpy and shifts the case into a higher count level, whereas at fixed current, increasing the gas flow lowers the enthalpy and shifts the case toward lower counts. In contrast, the apparent temperatures depend on the emissivity value specified to the camera software. Literature reports an emissivity range of $\varepsilon \approx 0.24$–0.31 for tungsten in the relevant temperature interval of 1500–2200 °C [26], which implies that the true emissivity varies between the experimental cases as the rod temperature most likely changes with the plasma generator operational settings. However, using a constant emissivity value, $\varepsilon = 0.30$, yields apparent temperatures between ~1550 °C and the upper calibration limit of the camera (2000 °C). For the highest-power cases (300 A, 50–55 Nm^3/h), the apparent temperature reaches beyond this limit; the underlying detector counts continue to increase, but the camera cannot convert them to temperatures above 2000 °C within this preset. When ε is lowered (e.g., to 0.28), cases with lower temperatures (~1500–1700 °C) still return valid readings, whereas hotter cases reach the calibration limit even earlier. This behavior reflects that emissivity and temperature are coupled, and neither can be assumed constant across operating conditions. Because of this, apparent temperatures must be interpreted with caution, while the counts remain directly comparable across the entire dataset. Overall, the correlation between gas enthalpy and detector counts supports the interpretation that the enthalpy of the plasma gas governs how much heat is convectively transported downstream and subsequently re-emitted as radiation from the tungsten surface. When the cases are grouped by specific gas enthalpy rather than by current or flow alone, consistent ordering of both axial radiative intensity and downstream tungsten heating emerges, confirming enthalpy as the governing parameter for thermal energy transport in the plasma jet.

Although the quantitative temperature mapping of the plume was limited by uncertainties in gas emissivity and IR camera constraints, the thermograms provide clear qualitative pictures of the plasma plume. A notable observation in cases with the 300 kW_{el} plasma generator is the appearance of a localized radial constriction near the generator outlet, where the plume appears to become narrower before re-expanding further downstream. This feature is referred to as "necking" in the paper. This constriction becomes more pronounced with increasing arc current, with estimates of the minimum plume diameter decreasing from about 14 mm at 200 A to around 6 mm at 300 A, based on IR-images. Increasing the CO_2 flow rate counteracts this narrowing to some extent, with the minimum diameter widening to approximately 9 mm at 300 A when the flow is raised from 50 to 55 Nm^3/h. Four representative cases are shown in Fig. 5, illustrating how current and flow jointly influence the degree of radial constriction.

To assess whether this phenomenon could be related to gas-dynamic effects, exit velocities were estimated from the volumetric flow rates and effective nozzle area, assuming a bulk exit temperature of 3500 K. Table 3 summarizes the calculated velocities together with corresponding Mach numbers. To place these values in context, the local speed of sound in CO_2 was estimated from the thermodynamic relation $\sqrt{\frac{\gamma RT}{Mw}}$ [27] where R is 8.313 J mol^{-1} K^{-1}, and γ for CO_2 is calculated based on thermophysical properties from NIST [28].

The resulting Mach numbers are therefore well below unity across all cases. The maximum velocity reached about 656 m/s at 55 Nm^3/h, corresponding to $M \approx 0.7$, while the lowest was 358 m/s at 30 Nm^3/h ($M \approx 0.4$). Since shock-cell structures and diamond patterns are known to arise at Mach numbers greater than 1 [27], their formation appears unlikely under the present conditions. However, given the uncertainty in the assumed bulk plasma temperature, a contribution from aerodynamic effects cannot be completely excluded. The observed constriction is nevertheless consistent with electromagnetic effects, where higher arc currents increase the self-induced magnetic field and compress the plasma column through Lorentz forces. Similar observations were reported by Polukhin et al. [29], who attributed radial constriction in high-current arcs to *Z*-pinch effects. While not quantitatively proven in the present study, the observed trends are consistent with this interpretation.

The presence of radial constriction also provides a physical explanation for the sharp intensity drop observed in the axial radiative measurements at 50 mm. At this location, the probe samples a reduced cross-section of the radiating plume, probably causing some of the emission to fall outside the line of sight. As the plume expands further downstream, the overlap increases, and measured intensities partially recover. In this way, IR imaging helps interpret the non-linear axial profiles and demonstrates how geometry affects radiative transfer measurements.

3.3. Discussion

The combined NAR and IR measurements establish two defining characteristics of the present CO_2-based plasma jet: (i) a highly localized near-field radiative core whose position and intensity depend sensitively on arc current and plume geometry, and (ii) sustained downstream thermal transport dominated by convection. The axial radiative intensity measurements demonstrate that line-of-sight emission is strongly influenced by plume constriction and spatial redistribution of the radiative zone, while infrared imaging confirms that substantial thermal energy persists downstream even when measured radiative intensity decreases locally. These experimentally resolved plume-scale features provide the physical basis for assessing how plasma heating differs from conventional combustion in industrial thermal systems.

The plasma–combustion comparison provides valuable insight into implications for process integration, such as in rotary kilns and glass furnaces. Within an enclosed geometry, the walls will partly reflect the radiation emitted from the plasma plume, amplifying the effective

Table 2
IR detector counts at the tungsten reference point for all 300 kW_{el} cases.

Case Id	Specific gas enthalpy (MJ/Nm^3)	Counts from IR	Temperature from IR (°C) ε = 0.30
P1	12.0	13,160	1847
P2	14.9	16,280	1953
P3	11.5	13,553	1543
P4	14.1	14,448	1681
P5	18.2	15,901	1900
P6	12.3	13,395	1519
P7	14.8	16,353	1964
P8	18.5	17,232	2000 (Saturated)
P9	14.1	15,057	1773
P10	17.0	17,086	2000 (Saturated)

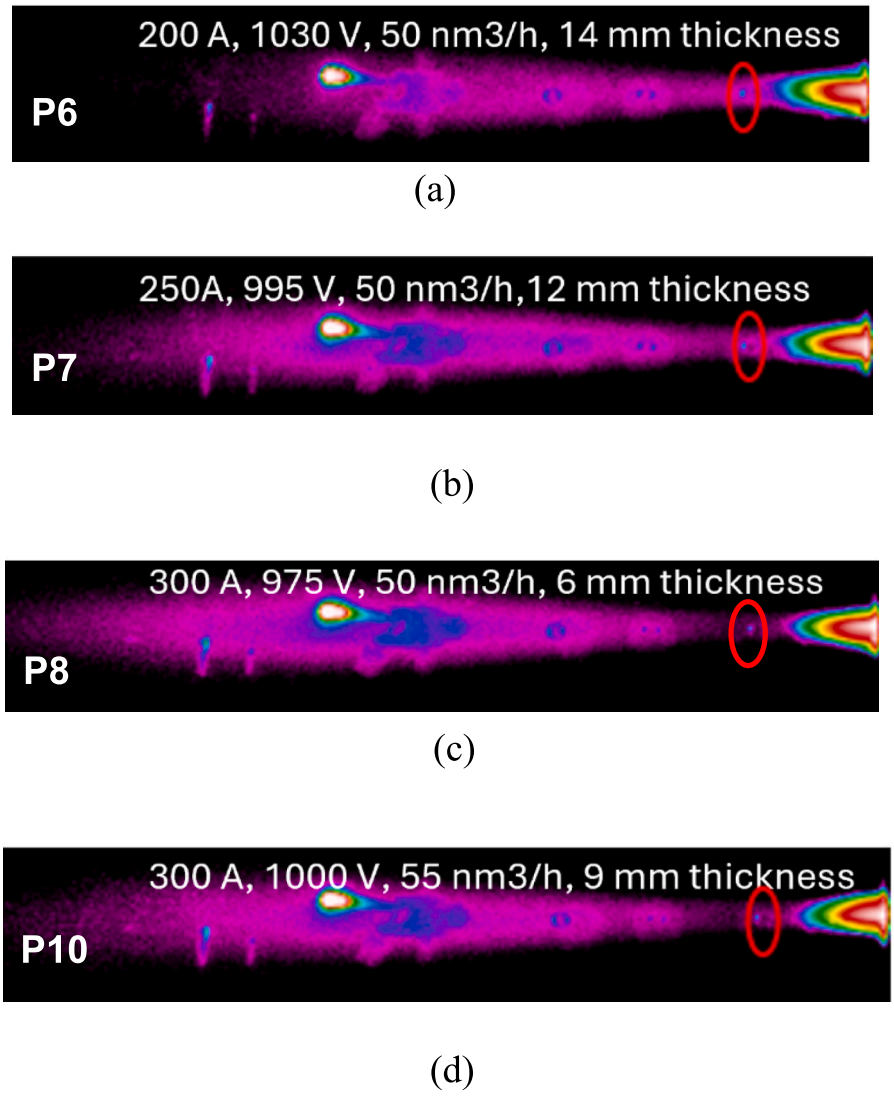

Fig. 5. IR thermographs of CO_2-based plasma plumes at 300 kW_{el} (a–d) showing neck formation under varying process conditions. Red circles highlight regions of radial constriction. (For interpretation of the references to colour in this figure legend, the reader is referred to the web version of this article.)

Table 3
Estimated plasma exit velocities for different CO_2 flow rates.

Volumetric flow rate (Nm^3/h)	Velocity (m/s)	Mach number
30	358	0.41
40	477	0.55
50	596	0.68
55	656	0.75

radiative field. In plasma heating, high radiative loads are concentrated near the burner tile compared to a combustion flame, requiring careful refractory selection and potential shielding in this region. Further downstream, convective transfer from the hot gas stream becomes increasingly important, enhancing mixing and heat delivery to the kiln charge over a longer residence time. The downstream thermal delivery is supported by the tungsten-count measurements. Even though a local minimum in line-of-sight radiative intensity occurs upstream, the rod located farther downstream still exhibits higher emitted-radiation counts that increase with specific gas enthalpy (Table 2). This indicates that substantial thermal energy is transported beyond the near-field radiative zone and transferred to surfaces predominantly through convection, followed by re-emission from heated tungsten surface. In enclosed thermal equipment such as rotary kilns and glass furnaces, this behavior implies a design trade-off between managing near-burner radiative hot spots through refractory selection and shielding and leveraging downstream convective heating for distributed process heat input.

The present results were obtained for a single non-transferred DC torch geometry at the 100–300 kWel scale and in open air, and the extent to which the observed intensity profiles and plume constriction transfer to MW-scale systems therefore requires caution. At larger power scales, changes in nozzle dimensions, arc attachment, current density, and gas throughput can alter both the characteristic length of the near-field radiative zone and downstream thermal transport. In confined environments, additional boundary effects are expected, including limited entrainment, altered jet development, and wall re-radiation, which can redistribute where heat is deposited relative to the burner tile and the charge. The present measurements should therefore be interpreted as benchmarks for local energy concentration and downstream heat transport for this torch concept, while scaling to MW operation and enclosed process equipment should be addressed through combined measurements and modelling under kiln-representative boundary conditions. Notably, the present torch concept has been demonstrated in a 300 kWel pilot kiln for clinker production, and scale-

up to 1 MW is being pursued within the same industrial development pathway [30].

By contrast, combustion flames provide lower near-field radiative intensity, as radiative emission is generally more spatially distributed due to extended luminous flame regions and the participation of soot and gas-phase emitters. When enclosed within kiln walls, view factors and re-radiation modify the balance, but the fundamental difference in energy distribution remains: plasma provides intense, localized radiation followed by convective energy transport, while combustion delivers more diffuse radiative heating. These distinctions must be considered in burner design, placement, and process optimization. The present dataset also provides a foundation for radiative-transfer modelling to resolve plume temperature fields under kiln-representative boundary conditions.

3.4. Idealized radiative transfer analysis

To demonstrate the practical usefulness of the experimental dataset and provide context for how it can support future modelling efforts, a set of idealized modelling examples are included in this work. The analysis examines the temperature conditions at the axial positions of the NAR probes required to reproduce the measured radiative intensities, and the aim is not to produce comprehensive predictions of the plasma jet temperature distribution, but to illustrate how access to high-quality measurements reduces uncertainty and supports the development and validation of more detailed future models.

The gas radiative properties are modelled on a spectral basis using the Malkmus Statistical Narrow-Band Model (SNBM) [31], with mean line spacing and mean line-intensity parameters for CO_2 and CO from the work of Rivière and Soufiani [32]. A discrete transfer method (DTM) is used to solve the radiative transfer equation, assuming the plasma jet occupies the central axis of an infinitely long cylindrical volume with axisymmetric temperature and composition. The model resolves the one-dimensional radiative intensity along a line of sight perpendicular to the jet axis and can be applied independently at each axial probe position. The boundary is prescribed as a cold black-body surface at ambient temperature (20 °C), representing the open-air surroundings without wall re-radiation. The modelling approach is described in detail by Johansson et al. [33]. Jet diameters at each axial position were estimated from the IR thermograms using the same binary image procedure applied in the necking analysis (Fig. 5), yielding 18, 29, and 37 mm at the second, third, and fourth NAR probe positions, respectively.

The extreme radiative intensities recorded at the first probe position (5 mm) cannot be reproduced within this modelling framework, as they exceed the achievable emission at the SNBM temperature limit of 5000 K. This may reflect even more extreme near-nozzle temperatures, or that the arc column extends partially beyond the torch exit as discussed in Section 3.1, neither of which is captured by an equilibrium gas radiation approach.

At the remaining three positions, peak temperatures are estimated by fitting the modelled line-of-sight intensity to the measured value. In the first, most simplified case, the plume cross-section is assumed to be isothermal and composed entirely of CO_2, returning peak temperatures of 1535, 1790, and 1520 K at the second, third, and fourth probe positions, respectively. In the second case, a parabolic radial temperature profile is prescribed, peaking on the jet axis and decreasing to ambient at the boundary. This yields respective peak temperatures of 2205, 2610, and 2185 K. The increase relative to the isothermal case reflects the attenuation of core emission by cooler peripheral gas, which requires a higher axial temperature to reproduce the same measured line-of-sight intensity. The temperature peak occurring at the third rather than the second probe position under both assumptions is attributed to the simplification of uniform CO_2 composition, which does not account for the reduction in radiatively active species due to dissociation at higher temperatures. In the third case, equilibrium CO_2 dissociation is incorporated, where the local CO_2 mole fraction decreases from the plume boundary inward as the temperature increases toward the axis. This yields peak temperatures of 2250, 2810, and 2215 K with equilibrium CO_2 mole fractions of 0.928, 0.602, and 0.938 at the second, third, and fourth probe positions, respectively. The temperatures are higher than in case 2 because CO, which forms as CO_2 dissociates, is a weaker radiative emitter than the CO_2 it replaces, and a higher peak temperature is therefore required to reproduce the same measured intensity. The temperature peak still occurs at the third probe position rather than the second, which is attributed to the high gas velocities and potentially extreme temperatures close to the nozzle, where the residence time may be insufficient for dissociation equilibrium to be fully established at the second probe position. As a further sensitivity check, the peak temperature at the second probe position was fixed at 2810 K, equal to the estimate at the third position, and the CO_2 mole fraction was used as the fitting parameter instead. This returns a CO_2 mole fraction of 0.362, indicating that a substantially higher degree of dissociation would be required at this position if temperatures comparable to those further downstream already prevail close to the nozzle exit. The estimated temperatures and CO_2 mole fractions for all three modelling cases are provided in the Supporting Information (Fig. S2).

The estimated peak temperatures of 2250 to 2810 K at the intermediate probe positions, together with the degree of CO_2 dissociation they imply, are relevant to high-temperature industrial applications. In enclosed systems such as rotary kilns and glass-melting furnaces, these temperature levels govern radiative loading on refractory materials near the burner tile, and the partial dissociation of CO_2 to CO along the jet raises the possibility of downstream CO re-oxidation contributing to the overall heat release within the kiln chamber. These results illustrate how the experimentally derived intensities can serve as practical constraints for temperature and composition inference, and support boundary condition selection in future, more detailed computational studies.

4. Outlook

The idealized radiative transfer analysis presented in Section 3.4 demonstrates one way in which the experimental dataset can be used to constrain estimates of peak temperature and CO_2 dissociation state along the plasma jet. Full characterization of the coupled temperature, species, and velocity fields requires CFD modelling incorporating plasma-specific thermophysical properties, arc-flow interactions, turbulent mixing, and radiation-flow coupling, conditions that demand spatially resolved boundary condition information currently beyond the scope of this experimental study. The observed transitions in heating modes, the onset of radial constriction, and the shifting emission zones provide critical benchmarks for model validation. Future numerical work could aim to replicate these behaviors under controlled boundary conditions, thereby improving predictive capabilities for plasma-assisted industrial processes. Further experimental work should focus on expanding temperature-resolved data within the plasma plume through new approaches capable of capturing local thermal gradients and temporal variations. Such efforts will enable more accurate comparison between experimental and numerical results and improve the understanding of energy transport mechanisms in plasma-assisted processes. By making these measurements available, the present study seeks to support coupling experimental plasma diagnostics with advanced simulations.

5. Conclusion

This work presents an experimental study of radiative heat transfer and plume morphology in CO_2-based thermal plasma plumes operated at two power scales 100–300 kW_{el}. Using narrow-angle radiometry and infrared thermography, the study characterizes axial radiative intensity distributions, their variation with arc current and gas flow rate, and discusses an observed necking phenomenon. The study provides novel measurement data of how operational parameter variation affects the radiative emissions from a plasma plume as well as observations of the

plasma plume geometry.

The work concludes with:

- Radiative intensity measurements using NAR identified localized heating zones near the burner outlet, with peak values exceeding 116 $kW/m^2 \cdot sr$ at 230 kW_{el} and 5 mm from the PG outlet. At higher currents, the reduced intensity measured at the same position indicates that the main emission zone can shift downstream, influenced by plume constriction and optical path alignment.
- Although radiative output decreases further downstream, IR imaging confirms that high gas temperatures persist, showing that energy transport continues predominantly through hot gas convection. This distinction between localized radiative heating near the outlet and convective energy delivery downstream is important for reactor design and thermal process optimization.
- A clear observation of a "necking phenomenon", where the neck diameter reduces as the current increases, confirming a threshold-like onset of radial plasma constriction.
- The visible thermal envelope of 300 kW_{el} PG captured via IR imaging extends further at higher currents, with plasma plumes delivering energy well beyond the burner outlet.

CRediT authorship contribution statement

Ibrahim Qasim: Writing – original draft, Visualization, Methodology, Investigation, Conceptualization. **Saumitra Mishra:** Writing – review & editing, Methodology, Conceptualization. **Adrian Gunnarsson:** Writing – review & editing, Supervision. **Fredrik Normann:** Writing – review & editing, Supervision. **Klas Andersson:** Writing – review & editing, Supervision.

Declaration of competing interest

The authors declare no competing financial interest.

Appendix A. Supplementary data

Supplementary data to this article can be found online at https://doi.org/10.1016/j.applthermaleng.2026.130994.

Data availability

No data was used for the research described in the article.

References

[1] S. Talekar, B.H. Jo, J.S. Dordick, J. Kim, Carbonic anhydrase for CO2 capture, conversion and utilization, Curr. Opin. Biotechnol. 74 (2022) 230–240, https://doi.org/10.1016/j.copbio.2021.12.003.

[2] H.S. Kwak, H.S. Uhm, Y.C. Hong, E.H. Choi, Disintegration of carbon dioxide molecules in a microwave plasma torch, Sci. Rep. 5 (2015) 18436, https://doi.org/10.1038/srep18436.

[3] J. Li, X. Zhang, J. Shen, T. Ran, P. Chen, Y. Yin, Dissociation of CO2 by thermal plasma with contracting nozzle quenching, J. CO_2 Util. 21 (2017) 72–76, https://doi.org/10.1016/j.jcou.2017.04.003.

[4] A. Bogaerts, G. Centi, Plasma technology for CO2 conversion: a personal perspective on prospects and gaps, Front. Energy Res. 8 (2020), https://doi.org/10.3389/fenrg.2020.00111.

[5] Y. Vadikkeettil, G. Ravi, K. Ramachandran, Prediction of operational characteristics of a dc non-transferred arc plasma torch using similarity criteria, Eur. Phys. J. D 71 (2017) 247, https://doi.org/10.1140/epjd/e2017-80207-6.

[6] Y. Xu, Q. Wei, H. Long, X. Zhang, S. Shang, X. Dai, Y. Yin, CO2 reforming of CH4 by synergies of binode thermal plasma and catalysts, Int. J. Hydrog. Energy 38 (2013) 1384–1390, https://doi.org/10.1016/j.ijhydene.2012.11.008.

[7] S. Mohsenian, M.S. Esmaili, B. Shokri, M. Ghorbanalilu, Physical characteristics of twin DC thermal plasma torch applied to polymer waste treatment, J. Electrost. 76 (2015) 231–237, https://doi.org/10.1016/j.elstat.2015.06.004.

[8] Y. Vadikkeettil, P. Amarnath, S. Yugeswaran, P.V. Ananthapadmanabhan, Comparative study of plasma torch characteristics using air and carbon dioxide, IEEE Trans. Plasma Sci. 50 (2022) 1395–1400, https://doi.org/10.1109/TPS.2021.3129593.

[9] P.R. Taylor, S.A. Pirzada, Thermal plasma processing of materials: a review, Adv. Perform. Mater. 1 (1994) 35–50, https://doi.org/10.1007/BF00705312.

[10] Bodil Wilhelmsson, Claes Kollberg, Johan Larsson, Jan Eriksson, Magnus Eriksson, CemZero–A Feasibility Study Evaluating Ways to Reach Sustainable Cement Production via the Use of Electricity, 2018.

[11] M. Zhukov, I. Zasypkin, Thermal Plasma Torches: Design, Characteristics, Application, Cambridge Int Science Publishing, 2007.

[12] C. Wang, Z. Zhang, H. Cui, W. Xia, W. Xia, Characteristics of helium DC plasma jets at atmospheric pressure with multiple cathodes, Chin. Phys. B 26 (2017) 085207, https://doi.org/10.1088/1674-1056/26/8/085207.

[13] M. Hrabovsky, M. Konrad, M. Hlina, V. Kopecky, T. Kavka, O. Chumak, A. Maslani, G. Van Oost, Plasma aided gasification of biomass and plastics using CO2 as oxidizer, in: International Symposium on Non-Thermal/Thermal Plasma Pollution Control Technology & Sustainable Energy, 2010. https://www.researchgate.net/publication/266672217.

[14] P. Amarnath, N. Nandy, B. Indumathy, S. Yugeswaran, Study on CO2 based thermal plasma torch and its effective utilization for material processing in atmospheric pressure, J. CO_2 Util. 66 (2022) 102290, https://doi.org/10.1016/j.jcou.2022.102290.

[15] T. Yang, J. Shen, T. Ran, J. Li, P. Chen, Y. Yin, Understanding CO_2 decomposition by thermal plasma with supersonic expansion quench, Plasma Sci. Technol. 20 (2018) 065502, https://doi.org/10.1088/2058-6272/aaa969.

[16] S. Yugeswaran, V. Selvarajan, Electron number density measurement on a DC argon plasma jet by stark broadening of Ar I spectral line, Vacuum 81 (2006) 347–352, https://doi.org/10.1016/j.vacuum.2006.06.001.

[17] A. Rida Galaly, G. Van Oost, N. Dawood, Sustainable plasma gasification treatment of plastic waste: evaluating environmental, economic, and strategic dimensions, ACS Omega 9 (2024) 21174–21186, https://doi.org/10.1021/acsomega.4c01084.

[18] R. Villarreal-Medina, A.B. Murphy, P.F. Méndez, M.A. Ramírez-Argáez, Heat Transfer Mechanisms in Arcs of Various Gases at Atmospheric Pressure, Plasma Chem. Plasma Process. 43 (2023) 787–803, https://doi.org/10.1007/s11090-023-10328-9.

[19] Y. Zhou, L. Zhu, B. Yang, L. Fan, X. Meng, R. Chu, X. Jiang, P. Li, W. Li, H. Chen, Heavy metal migration regimes in the production of syngas from solid waste by thermal plasma treatment, J. Hazard. Mater. 461 (2024) 132698, https://doi.org/10.1016/j.jhazmat.2023.132698.

[20] A.B. Murphy, H. Park, Modeling of thermal plasma processes: the importance of two-way plasma-surface interactions, Plasma Process. Polym. 14 (2017), https://doi.org/10.1002/ppap.201600177.

[21] J. Ko, T.-H. Kim, S. Choi, Numerical simulation of cement Kiln combined with thermal plasma for SF_6 pyrolysis, Appl. Sci. Converg. Technol. 28 (2019) 93–100, https://doi.org/10.5757/ASCT.2019.28.4.93.

[22] G. Bonizzoni, E. Vassallo, Plasma physics and technology; industrial applications, Vacuum 64 (2002) 327–336, https://doi.org/10.1016/S0042-207X(01)00341-4.

[23] Z. Zhang, Q. Gou, T. Zhang, X. Lu, L. Xu, J. Zhang, Simulation and analysis of the heat transfer mechanism of arc plasma with CMT plus pulse composite heat source, Weld. World 68 (2024) 525–541, https://doi.org/10.1007/s40194-023-01594-4.

[24] A. Gleizes, J.J. Gonzalez, P. Freton, Thermal plasma modelling, J. Phys. D. Appl. Phys. 38 (2005) R153–R183, https://doi.org/10.1088/0022-3727/38/9/R01.

[25] K.S. Mujumdar, V.V. Ranade, Simulation of rotary cement kilns using a one-dimensional model, Chem. Eng. Res. Des. 84 (2006) 165–177, https://doi.org/10.1205/cherd.04193.

[26] Bramson Mikaël' A., Infrared Radiation, Springer Publishing New York Inc., 2013.

[27] D. John, Anderson, Modern Compressible Flow : With Historical Perspective, 3rd ed., McGraw-Hill, New York, 2020.

[28] P.J. Linstrom, W.G. Mallard, NIST Chemistry WebBook, NIST Standard Reference Database Number 69, National Institute of Standards and Technology, 2025.

[29] S.N. Polukhin, A.E. Gurei, V.Ya. Nikulin, E.N. Peregudova, P.V. Silin, Studying how plasma jets are generated in a plasma focus, Plasma Phys. Rep. 46 (2020) 127–137, https://doi.org/10.1134/S1063780X20020087.

[30] Heidelberg Materials Northern Europe, Major Breakthrough for Plasma-Heated Cement Kiln in Sweden, Heidelberg Materials (News/Press Release), 2026.

[31] W. Malkmus, Random Lorentz band model with exponential-tailed S^−1 line-intensity distribution function*, J. Opt. Soc. Am. 57 (1967) 323, https://doi.org/10.1364/JOSA.57.000323.

[32] P. Rivière, A. Soufiani, Updated band model parameters for H2O, CO2, CH4 and CO radiation at high temperature, Int. J. Heat Mass Transf. 55 (2012) 3349–3358, https://doi.org/10.1016/j.ijheatmasstransfer.2012.03.019.

[33] R. Johansson, B. Leckner, K. Andersson, F. Johnsson, Influence of particle and gas radiation in oxy-fuel combustion, Int. J. Heat Mass Transf. 65 (2013) 143–152, https://doi.org/10.1016/j.ijheatmasstransfer.2013.05.073.